AIAA JOURNAL
Vol. 46, No. 11, November 2008

Improved Model for the Penetration of Liquid Jets in Subsonic Crossflows

A. Mashayek,* A. Jafari,* and N. Ashgriz†
University of Toronto, Toronto, Ontario M5S 3G8, Canada

DOI: 10.2514/1.28254

A theoretical model for the penetration of a liquid jet in subsonic gaseous crossflow is developed. The model allows for the deformation of the jet cross section from circular to elliptic shapes along its path. A force balance analysis on an elliptical liquid element is performed. Aerodynamic, viscous, and surface tension forces are considered counting for the nonlinear terms at large deformations. The effect of mass shedding is also included in the model. This effect changes the jet trajectory and deformation at higher Weber numbers. In addition, the drag coefficients of elliptical cylindrical elements with different aspect ratios are calculated numerically for a range of Reynolds numbers. It is observed that the drag coefficient of the cylindrical element changes considerably with Reynolds number and the jet deformation. The change in the drag force considerably affects the jet deflection in the gas stream. Results show that the liquid-to-gas momentum ratio is not the only governing parameter in predicting the jet trajectory. Gas Weber number, rate of mass shedding from the jet, jet cross-sectional deformation, variation in the drag coefficient, and variation in the liquid and gas properties all affect the jet penetration.

Nomenclature

A	=	lateral area of the cylindrical element
a	=	semimajor axis of an ellipse
b	=	semiminor axis of an ellipse
C_D	=	drag coefficient
C_{dis}	=	discharge coefficient
d	=	round jet exit diameter
d_{eq}	=	equivalent diameter defined as $2 \times r_{\text{eq}}$
d_0	=	initial diameter of the cross section of the jet
e	=	ratio of the minor axis of an ellipse to its major axis, b/a
F_{aero}	=	aerodynamic force acting on the element
F_p	=	pressure force acting on the element
F_s	=	surface tension force acting on the element
F_{shear}	=	shear force acting on the element
F_v	=	viscous force acting on the element
h	=	element thickness
m_{elem}	=	mass of the cylindrical element
p	=	ambient pressure
p_0	=	atmospheric pressure (reference value)
q	=	momentum ratio
Re	=	Reynolds number, $\rho u d/\mu$
Re_g	=	Reynolds number based on gas properties, $\rho_g u_{\text{rel}} d_{\text{eq}}/\mu_g$
R_M	=	ratio of the mass of the cylindrical element to that of a droplet with the same equivalent radius
r	=	radius of the cross section of the jet
r_{eq}	=	equivalent radius of the cross section of the jet defined as $(a \times b)_{0.5}$
r_0	=	initial radius of the cross section of the jet
T_0	=	atmospheric temperature
T_∞	=	temperature of the gas stream
t_s	=	time elapsed from the start of stripping
t^*	=	characteristic aerodynamic time
U	=	velocity
U_x	=	velocity component of the element in the direction of the gas flow
U_z	=	velocity component of the element in the cross-streamwise direction
u_g	=	gas velocity
v_j	=	jet velocity
u_{rel}	=	relative velocity of the gas to the element
W	=	work
We	=	Weber number
We_{crit}	=	critical Weber number which sets the limit for start of mass stripping
We_g	=	gas Weber number, $\rho_g u_g^2 d/\sigma$
We_{local}	=	local gas Weber number, $\rho_g u_g^2 (2a)/\sigma$
X	=	gas streamwise distance from the nozzle
Z	=	injection streamwise distance from the nozzle
θ	=	angle of deflection of the liquid column
μ_g	=	gas viscosity
μ_j	=	jet viscosity
ξ	=	distance between the center of the cylindrical element and the center of mass of the half-element
ρ_g	=	gas density
ρ_j	=	jet density
σ	=	liquid surface tension

Subscripts

aero	=	aerodynamic
b	=	breakup location
cm	=	center of mass
crit	=	critical
elem	=	element
g	=	gas stream property
j	=	liquid jet property
local	=	local
p	=	pressure
rel	=	relative to the element
s	=	surface
shed	=	shedding
shear	=	related to shear force
ub	=	upper boundary
v	=	viscous
∞	=	main gas stream property

Received 13 November 2006; revision received 2 June 2008; accepted for publication 10 July 2008.

*Graduate Research Assistant, Department of Mechanical and Industrial Engineering.

†Professor, Department of Mechanical and Industrial Engineering, Corresponding Author; ashgriz@mie.utoronto.ca.

I. Introduction

RADIAL injection of liquid jets into a high-velocity and temperature cross-stream at elevated pressures has various applications in fuel injection systems and advanced aircraft engines, such as gas turbines, afterburners, augmenters, and ramjet–scramjet combustors. This type of radial fuel injection into a crossflow improves fuel atomization and vaporization characteristics and is commonly used in turbojet augmenter sections and rich, burn-quick, quench-lean burn, lean premixed prevaporized, and ramjet and scramjet combustion systems.

To date, several analytical, experimental, and numerical studies have investigated various characteristics of the jet-in-crossflow (JICF) atomization. Each of the experimental works has focused on a specific range of flow parameters. Several correlations have been developed based on the experimental data to predict various features of the JICF atomization. Because of the nature of experimental studies, their results and correlations are mainly applicable within the specific range of their test conditions.

The jet-in-crossflow atomization problem involves very complex flow physics, such as strong vortical structures, small-scale wave formation, stripping of small droplets from the jet surface, and formation of ligaments and droplets with a wide range of sizes. The atomization mechanism is well believed to start by the growth of the waves that form on the surface of the jet after injection from the nozzle. The relative velocity between the gas and the liquid phase amplifies the surface waves up to the point where the jet breaks up into smaller droplets due to the aerodynamic forces. From the computational point of view, the complete numerical simulation of such a problem, resolving most important flow scales on the Eulerian frame, is not still economically feasible, especially for industrial applications. These issues signal the demand for some simpler, yet reliable, models that can be used for industrial design purposes and, at the same time, can take into account important parameters, such as flow conditions and physical properties of the liquid and gas phases. An alternative to the Eulerian methodology is to track the droplets in Lagrangian formalism, which is computationally much more affordable and can be used in industrial design processes. One of the first works to address the JICF problem was the work of Reitz [1]. He modeled the atomization mechanism by estimating the wavelength and growth rate of the surface waves and relating the breakup droplet sizes to the wavelengths. The liquid jet was modeled by continuous injection of parent droplets with sizes equal to the nozzle diameter. Liu et al. [2] similarly modeled the liquid jet by successive injection of droplets into the gas stream and investigated the effects of the crossflow on the penetration of the water jet and the secondary breakup of the droplets. However, less care was taken in their study in distinguishing the parent drops from the product drops compared to the work of Reitz [1]. As reported by Reitz, this distinction plays an important role in the atomization process, liquid phase vaporization, and the resulting droplet distribution. Liu et al. [2] tracked the particles in the Lagrangian frame and used the Taylor analogy breakup (TAB) [3] model to determine the size of droplets formed due to the secondary breakup of the parent droplets. They concluded that the TAB model can qualitatively predict the effects of various physical parameters, however, it significantly underpredicts the drop size. This might be partly due to not discriminating between the parent and product droplets and also due to the fact that several flow structures associated with the liquid column are neglected once the jet is replaced by a sequence of droplets. In reality, the vortical structures formed due to the presence of the liquid column play a great role on the secondary breakup of the droplets and ligaments shed from the column. Direct injection of droplets from the nozzle (instead of a liquid jet) exposes the droplets directly to the freestream gas flow, leading to rapid breakup of the parent droplets and incorrect size distribution. Rachner et al. [4] developed a numerical scheme to predict the jet penetration by treating the liquid jet as a cylinder deflected by the airstream. They modeled the atomization mechanism by considering a characteristic time criterion for the liquid column breakup, modeling the shear breakup of the liquid column and its fragments by liquid boundary-layer stripping, and tracking the particles in the Lagrangian frame. Madabhushi [5] also developed a numerical model to predict the jet atomization characteristics in a subsonic crossflow. Their model simulated several features of the JICF atomization, including the effects of the jet deflection, droplet secondary breakup, and change in the drag coefficient due to deformation, among others.

Khosla and Crocker [6] also performed a similar analysis using the TAB [3] model by injecting droplets from the nozzle. However, droplets were restrained from breaking up until some imposed time. The drag coefficient of the droplets was set to be equal to an empirical value, that of a liquid jet, to force the droplets to follow the trajectory of the liquid jet. This method helped predict the penetration of the liquid phase in the gas phase. However, no size information was provided in their study [6].

We now propose a new method for modeling the atomization of a liquid jet in a crossflow. In this method, an obstacle of a shape similar to a continuous liquid jet is constructed. This obstacle allows for the development of vortical structures on the leeward of the liquid jet. Then, droplets can be injected from different locations along the obstacle edge, that is, the trajectory of the liquid jet. This is an improved physical model for the mass stripping from the liquid column that incorporates the effects of the presence of the liquid column on secondary breakup. Particles shed from the jet and particles produced after the breakup of the liquid column can then be tracked in the Lagrangian formalism, whereas the presence of the jetlike obstacle helps develop a realistic flowfield. This procedure can be used to predict the droplet size, velocity distribution, and mass flux for different JICF conditions. To develop this relatively fast method, several submodels are needed, which can be divided into three main categories: 1) models that predict the column deformation, jet trajectory, maximum penetration, and column breakup times and locations; 2) models that provide information regarding the primary breakup of the liquid column (mass stripping) and the formation of droplets and ligaments; 3) models that deal with the secondary breakup of the ligaments and drops, that is, the atomization process.

The present article focuses on calculating the trajectory and shape of the continuous liquid jet by developing a theoretical model for predicting the jet deformation and penetration. Details of the theoretical model are provided and results for different cases at various conditions are presented, discussed, and compared with the available data in the literature. To obtain an insight into the problem and the parameters involved, the following section presents a brief review of a number of studies on the penetration of liquid jets in subsonic crossflows. However, this is by no means an exhaustive list of the works done on this problem. A more comprehensive review of the studies related to jet trajectory and penetration can be found in Lin et al. [7]. The correlations presented in the following section are mainly chosen for comparison purposes.

II. Literature Review

Schetz and Padhye [8] experimentally studied the penetration and breakup of liquid jets in subsonic gas streams using optical measurement techniques. They correlated their penetration data using parameters suggested by a theoretical analysis and came up with the following correlation for maximum penetration:

$$\left(\frac{z_{\max}}{d}\right) = C\sqrt{q}C_{\text{dis}}\left(\frac{d_{\text{eq}}}{d}\right) \tag{1}$$

where d is the nozzle diameter, $z_{\max}$ represents the maximum penetration, C is a constant that incorporates the drag coefficient, C_{dis} is the discharge coefficient of the fuel orifice, and d_{eq} is the equivalent injector diameter that is equal to one for a circular injector. In most of the following correlations for jet trajectory and maximum penetration, the equations are nondimensionalized by diameter d, like Eq. (1). The liquid-to-gas momentum ratio q is defined as

$$q = \frac{(\rho u^2)_j}{(\rho u^2)_g} \tag{2}$$

Chen et al. [9] used a laser-sheet imaging technique to study the effect of momentum ratio on the jet penetration. They changed the momentum ratio from 3 to 45 at room temperature, at pressures between 1 and 2 bars, and at a Mach number of 0.4. Their final correlation is in the following form:

$$\frac{z}{d} = 9.91(q)^{0.44}\left[1 - \exp\left(\frac{-x/d}{13.1}\right)\right]\left[1 + 1.67\exp\left(\frac{-x/d}{4.77}\right)\right] \times \left[1 + 1.06\exp\left(\frac{-x/d}{0.86}\right)\right] \tag{3}$$

Wu et al. [10] provided a phenomenological model for the jet penetration, based on experiments using the shadowgraph technique. Their measurements were at normal temperature and pressure with momentum ratios in the range of 4–185 and Mach numbers of 0.2–0.4. They modeled the liquid jet as a circular column and applied a simple force balance to obtain the jet trajectory using a regression analysis yielding the following correlations:

Liquid column trajectory

$$\frac{z}{d} = 1.37\sqrt{q(x/d)} \tag{4}$$

Height of the column breakup point

$$\frac{z_b}{d} = 3.44\sqrt{q} \tag{5}$$

Gas streamwise distance to the column fracture point

$$\frac{x_b}{d} = 8.06 \tag{6}$$

where z and x correspond to cross-streamwise (normal to gas stream) and streamwise (in the direction of gas stream) distances from the injector, respectively. The subscript b corresponds to the breakup location of the jet where it disintegrates as a whole. Wu et al. [11] extended their work and studied other characteristics of the jet in crossflows, such as the spray width and the liquid mass distribution. They offered the following equation for the maximum spray penetration z:

$$\frac{z}{d} = 4.3q^{0.33}\left(\frac{x}{d}\right)^{0.33} \tag{7}$$

Inamura et al. [12] experimentally investigated the wave characteristics and spray characteristics of liquid jets and slurry jets injected transversely into subsonic airstreams. Among the various characterizations performed in their study, the following two correlations were offered for jet penetration:

For water jets

$$\frac{z}{d} = (1.18 + 0.24d)q^{0.36}\,\ell_n\left(1 + (1.56 + 0.48d)\frac{x}{d}\right) \tag{8}$$

For slurry jets

$$\frac{z}{d} = (1.17 + 0.16d)q^{0.43}\,\ell_n\left(1 + (0.75 + 0.95d)\frac{x}{d}\right) \tag{9}$$

Heister et al. [13], Li and Karagozian [14], Nguyen and Karagozian [15], and Inamura [16] calculated the jet trajectory by assuming that the jet cross section changes from a circle at injection point to an elongating ellipse with its major axis perpendicular to the crossflow. This assumption was made to take into account the effects of crossflow-induced deformation on the jet trajectory. Nguyen and Karagozian [15] offered an analytical/numerical model that predicted the behavior of nonreacting and reacting liquid jets injected in subsonic crossflows. The mass loss due to boundary-layer shedding, evaporation, and combustion was calculated and incorporated in their trajectory calculations.

Inamura [16] calculated the jet trajectory using the elliptic cross section assumption. He employed Clark's [17] equations, derived for small deformations of a 2-D droplet, to model the jet deformation. Not taking into account the nonlinearities due to large deformation of the liquid column, as well as neglecting the effects of mass stripping and variations in the drag coefficient, led to the prediction of the jet trajectory only up to locations far before the jet's disintegration point. Becker and Hassa [18] applied shadowgraphs, MIE-scattering calculation, and phase Doppler techniques to study various characteristics, such as the liquid flux and droplet size distributions at different locations. Their experiments were carried out at momentum ratios of 1–40, pressures of 1.5–15 bars, and at normal temperatures. Their correlation for near-field penetration of the jet is

$$\frac{z}{d} = 1.48q^{0.42}\,\ell_n\left(1 + 3.56\frac{x}{d}\right) \qquad (1 < q < 40, 90 < We_g < 2120, 2 < x/d < 22) \tag{10}$$

Masuda et al. [19] studied transverse injection of a recessed liquid jet into a high-speed crossflow at pressures between 3.7 and 6.4 atm and temperatures between 350 and 475 K. The air Mach numbers were between 0.25 and 0.33, with momentum ratios of 2–30. High-speed, short-exposure digital shadowgraph pictures were captured to document the behavior of the spray jet. They proposed the possible effects of discharge coefficient and differences in geometries of the test sections on the penetration and general shape of the spray plume. They predicted the penetration of the spray through the following correlation:

$$\frac{z}{d} = 0.92q^{0.50}\left(\frac{x}{d}\right)^{0.33} \qquad (2 < q < 30) \tag{11}$$

Lakhamraju and Jeng [20] studied the nature of breakup and penetration of liquid jets injected transversely in subsonic crossflows at elevated temperatures, using a pulsed shadowgraph technique at momentum ratios of 1–50, Mach numbers of 0.2–0.9, temperatures of 363–505 K, and atmospheric pressure. They reported that an increase in airstream temperature results in a decrease in the liquid jet penetration. A correlation including the effect of temperature was offered in the following form:

$$\frac{z}{d} = 1.8444q^{0.546}\,\ell_n\left[1 + 1.324\left(\frac{x}{d}\right)\right]\left(\frac{T_\infty}{T_0}\right)^{-0.117} \tag{12}$$

Elshamy and Jeng [21] investigated the effect of pressure on the spray boundaries. Their tests were conducted at air velocities of 39–306 m/s, pressures up to 7 bar, liquid-to-gas momentum ratios of 2–71, and room temperature. Flow visualizations were carried out using pulse shadowgraphy. Their study concluded that the increase in the ambient pressure leads to a slight decrease in the penetration of the jet, rise in the lower boundary of the jet, and reduction in the spray coverage area. The upper-boundary correlation matched their experimental data reasonably, whereas the lower one showed a relatively large deviation. This was attributed to the droplets stripped off from the liquid column making the visualization more difficult at the lower boundary. Two correlations were proposed for the upper and lower boundaries of the spray as follows:

Upper boundary

$$\frac{z}{d} = 4.95\left(\frac{x}{d} + 0.5\right)^{0.279} q^{0.424}We^{-0.076}\left(\frac{p}{p_0}\right)^{-0.051} \tag{13}$$

Lower boundary

$$\frac{z}{d} = 4.26\left(\frac{x}{d} - 0.5\right)^{0.349} q^{0.408}We^{-0.30}\left(\frac{p}{p_0}\right)^{0.111} \tag{14}$$

As shown by Eqs. (13) and (14), Elshamy and Jeng [21] incorporated the Weber number in their correlations. Among the first who included the effect of the Weber number in their correlation are Stenzler et al. [22]. They found that, in addition to the momentum ratio, the Weber number and liquid viscosity also play a role in the jet penetration.

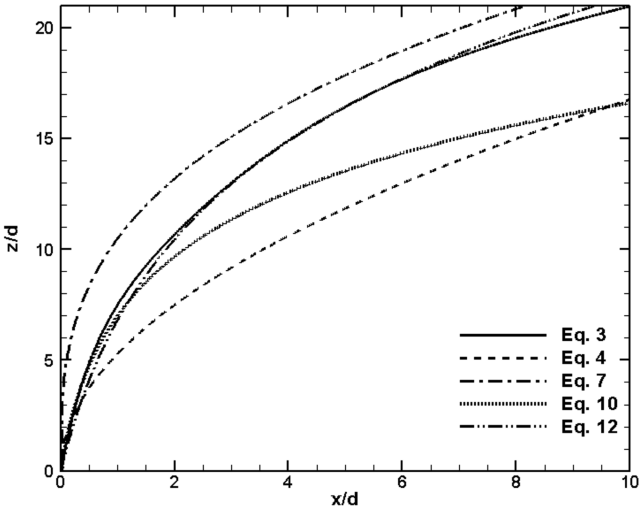

Fig. 1 Jet trajectories calculated using several correlations for a case with momentum ratio q of 15.

Figure 1 shows the jet trajectories predicted by Eqs. (3), (4), (7), (10), and (12) for a sample momentum ratio of 15. The obvious discrepancies between the predicted curves can be partly due to experimental uncertainties and difficulties in defining the boundaries of the liquid jet, especially for cases with a high rate of mass stripping. Also, the specific experimental details and flow conditions behind each correlation must be considered in interpretation of the curves. Figure 1 confirms that the correlations can have considerable deviation from reality when applied to test conditions far from their own. Furthermore, it is evident that the liquid-to-gas momentum ratio, which is the only parameter incorporated in the curves of Fig. 1, cannot be the only factor in determination of the jet penetration. Several test conditions and physical properties must be specified and included in the calculations. Providing correlations that count for all the governing parameters demands an extremely wide range of experiments. Thus, it is the objective of the present study to develop a model that takes into account more physical parameters which play effective roles in the jet-in-crossflow atomization.

III. Model

The model presented in the following sections can be generally divided into four sections. First, the basic equation of deformation of the jet cross section is derived. Second, the equation for the jet trajectory is obtained. Third, the mass reduction from the jet is discussed. Finally, the time-varying drag coefficient is calculated and implemented in the equations.

A. Jet Deformation

The first step in modeling the jet behavior involves deformation of the liquid column. To analyze the deformation of the liquid column in the uniform crossflow, a cylindrical element of infinitesimal thickness h from the liquid column is assumed, as shown in Fig. 2a. At any point, the element is perpendicular to the path its center of mass travels. The spatial location of this element as it moves along the jet trajectory is illustrated in Fig. 2a. Figure 2b shows the coordinate of the center of mass of the liquid element and the coordinate of the upper boundary of the jet.

The element is deformed and moved along the jet trajectory due to the interplay between aerodynamic, surface tension, and viscous forces. We assume that the jet cross section changes from a circle to an ellipse. In reality, however, the jet cross section changes slightly into a kidney shape [15]. The ellipse aspect ratio e, defined as the ratio of the ellipse minor axis b to its major axis a, decreases with time until the breakup location. It should be noted that this assumption is only an approximation to the actual deformation of the liquid jet and, as will be shown in the results, it provides enough precision to predict the jet penetration with acceptable accuracy.

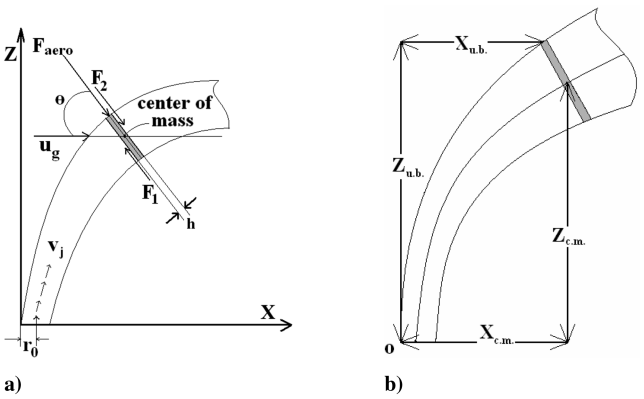

Fig. 2 Schematic of the jet element movement along the trajectory: a) direction of the forces and velocities involved; b) center of mass and the upper-boundary coordinates.

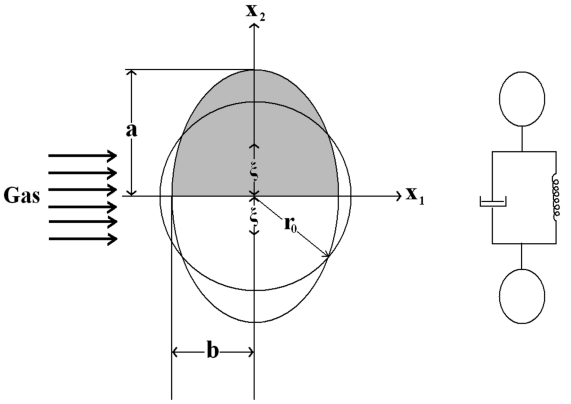

Fig. 3 Analogy between an oscillating two-dimensional drop and a forced mass-spring system [17].

Based on the work of Clark [17], the deformation of a 2-D liquid droplet is assumed to depend on the viscous (dissipative) force, the interfacial tension (restoring) force, and the inertial force. Clark modeled the small deformations of drops by calculating the linearized terms for the three forces based on the analogy between an oscillating two-dimensional droplet and a forced mass-spring system, as shown in Fig. 3. Using the same analogy and performing a force balance in the x_2 direction (Fig. 3) of the cross-sectional plane leads to the equation for the oscillation of the element in the form of

$$F_p + F_v + F_s = m_{\text{elem}}\ddot{\xi} \tag{15}$$

Formulating the element deformation in terms of the motion of the center of mass of the half-element, Clark [17] obtained the viscous force by dividing the energy dissipation per unit thickness of the element by $2d\xi$, where $d\xi$ is the increment of ξ, the distance from the center of mass of the whole droplet to the center of mass of the half-droplet. This distance is given by $4a/3\pi$ for elliptic cross sections and $4r_0/3\pi$ for the initial circular section. Applying the nonlinearized 2-D viscous force offered by Clark for large deformations of an elliptic cross section, we have

$$F_v = -2\pi\mu_j r_{\text{eq}}^2 h\left(\frac{d\xi/dt}{\xi^2}\right) \tag{16}$$

where μ_j is the liquid viscosity and r_{eq} is the radius of a circle with equal area to that of the instantaneous elliptic cross section and is given by $(a \times b)^{0.5}$. As will be explained in the mass reduction section, the initial cross-sectional area of πr_0^2 will not remain constant as the element moves along the jet trajectory. The surface tension force acting through the center of mass of the half-element is [17]

$$F_s = -\left(\frac{1}{2}\right)\sigma\frac{dA}{d\xi} \tag{17}$$

where σ is the liquid surface tension, A is the lateral surface area of the element shown in Fig. 2a, which is the product of the instantaneous perimeter of the elliptical cross section and the element thickness. Using Cantrell's formula for the circumference of an ellipse [18], the lateral surface area of the element is

$$A = h \times [4(a+b) - 2(4-\pi)ab/H] \tag{18}$$

where H is

$$H = [(a^m + b^m)/2]^{1/m} \tag{19}$$

In practice, the value of 0.825 (33/40) for the exponent m yields an error of less than 0.0085% for any ellipse.[‡] By differentiating Eq. (18), noting that $\xi = 4a/3\pi$ and $ab = r_{eq}^2$, and substituting into Eq. (17), the surface tension force acting through the center of mass of the half-element becomes

$$F_s = -\sigma \times h \times \frac{3\pi}{8}\left[4(1 - r^2a^{-2}) + \frac{c}{d}\right] \tag{20}$$

where the constants c and d are

$$c = 2r^2(4-\pi)(a^{m-1} - r^{2m}a^{-m-1}) \tag{21}$$

$$d = 2\left(\frac{a^m + r^{2m}a^{-m}}{2}\right)^{(m+1)/m} \tag{22}$$

It should be noted that, in differentiating Eq. (18), it is assumed that the rates of change of the cross section axes a and b, due to jet deformation, are much larger than the change in the equivalent cross section radius r_{eq} due to mass stripping. This can justify the constant r_{eq} assumption made during the differentiation.

The work done on the whole element due to external pressure is [23]

$$dW = -\frac{1}{2}pA_p d\xi \tag{23}$$

where A_p is the frontal area of the element ($b \times h$), and p is the gas stagnation pressure:

$$\frac{1}{2}\rho_g u_{rel}^2 \tag{24}$$

where u_{rel} is the relative velocity of the gas to the element. Because the gas velocity vector does not always lie on the element plane, the projected component of the gas velocity should be considered in calculating the aerodynamic force F_{aero}. The normal component u_g lies in the direction of F_{aero}, as shown in Fig. 2a. Thus, the relative velocity can be written as

$$u_{rel} = u_g \cos(\theta) \tag{25}$$

where θ is the angle between the gas stream direction and the plane of the element. By substituting Eqs. (24) and (25) into Eq. (23), and dividing both sides by $d\xi$, we get

$$F_p = \frac{dW}{d\xi} = \frac{1}{2}\rho_g bh[u_g \cos(\theta)]^2 \tag{26}$$

Projecting the velocity onto the cross-sectional plane, as done in Eq. (25), is a key step in the modeling process. Incorporating the main stream velocity u_g in Eq. (26), rather than the projection term $u_g \cos(\theta)$, leads to overestimation of the total force exerted on the element which, in return, leads to overestimating the cross-sectional deformation. As will be shown in the next section, the drag coefficient changes noticeably with an increase in the aspect ratio. Thus, overpredicting the drag force also has a negative effect on the instantaneous values of the drag coefficient, which emphasizes the importance of Eq. (25). By substituting Eqs. (16), (20), and (26) into Eq. (15), using $m_{elem} = 0.5\rho_j\pi abh$ for the half-element, and dividing all the terms by the element thickness h, the final form of the equation of deformation of the liquid jet becomes

$$c_1\left(\frac{d^2\xi}{dt^2}\right) + c_2\left(\frac{d\xi}{dt}\right) + c_3 = c_4 \tag{27}$$

where c_1 through c_4 are defined as

$$c_1 = \frac{1}{2}\rho_j\pi ab, \qquad c_2 = \left(\frac{2\pi\mu_j ab}{\xi^2}\right)$$

$$c_3 = \sigma \times \frac{3\pi}{8}\left[4(1 - r^2a^{-2}) + \frac{c}{d}\right], \qquad c_4 = \frac{1}{2}\rho_g b[u_g \cos(\theta)]^2$$

B. Jet Trajectory

In this section, we perform a force balance in the X–Z plane to obtain the jet trajectory. Figure 2a shows the chosen coordinate system with the origin located at the left corner of the injection nozzle. This choice has been made to write the equation of trajectory for the windward boundary of the liquid jet rather than its centerline. It should be noted that, in this section, the force balance is performed on the whole element, unlike the previous section. F_{aero} is the aerodynamic force due to the gas flow. As shown in Fig. 2a, F_1 is the shear force exerted on the element from the lower element, and F_2 is the shear force from the upper element. The aerodynamic force is

$$F_{aero} = \frac{1}{2}C_D\rho_g u_{rel}^2 A \tag{28}$$

Using Eq. (25), and noting that $A = 2a \times h$, Eq. (28) becomes

$$F_{aero} = C_D ah\rho_g[u_g \cos(\theta)]^2 \tag{29}$$

Similar to Inamura [16], we assume the jet velocity along the trajectory to be constant and equal to the initial injection velocity. This assumption is reasonably valid up to the breakup location. Thus, the velocity of the center of mass of the element can be written in the form of

$$u_x = v_j \sin(\theta) \tag{30}$$

$$u_y = v_j \cos(\theta) \tag{31}$$

Balancing the forces in the X direction for the *full element*, we get

$$m_{elem}\ddot{x} = F_{aero}\cos(\theta) - (F_1 - F_2)\cos(\theta) \tag{32}$$

Differentiating Eq. (30) with respect to time, setting it equal to Eq. (32), and solving for θ, we get the equation for jet curvature angle with respect to time:

$$\frac{d\theta}{dt} = \frac{(F_{aero} - F_{shear})}{\rho_j\pi abhv_j} \tag{33}$$

where F_{shear} is the resultant of the shear force exerted on the element from the neighbor elements. A simplified model for the shear force between the adjacent elements of small enough thickness is obtained as

$$F_{shear} = F_1 - F_2 = \pi ab\mu_j v_j \kappa \sin(d\theta)/d\theta \simeq \pi ab\mu_j v_j \kappa \tag{34}$$

where κ is the local curvature of the jet trajectory.

It should be noted that a small error enters the calculations by writing Eq. (32) in the noninertial reference frame attached to the cross-sectional element. To address this problem, one should add the necessary correction terms to the equation. The correction or

[‡]http://home.att.net/~numericana/answer/ellipse.htm

fictitious terms consist of two groups. The first group is due to the linear acceleration of the center of the moving coordinate with respect to a global inertial frame, and the second group is associated with the angular rotation of the noninertial frame. In the present calculations, the former is added to the equations, as will be shown. The latter has a negligible contribution in cases with high momentum ratio because the rotation rate of the element is small compared to its translational acceleration. However, this effect should be considered for small momentum ratios. The angular velocity and acceleration of the moving frame can be calculated for this purpose by using Eq. (33).

C. Mass Reduction

As the jet moves along its trajectory, droplets and fragments strip from the liquid column. The rate of mass stripping at different heights of the liquid column strongly depends on the gas flow conditions and the breakup regime. Wu et al. [10] and Becker and Hassa [18] classified the breakup regime with respect to the gas Weber number. Their studies demonstrated that at low Weber numbers, the breakup type is bag or bag-shear. However, as the Weber number increases, the shear breakup regime is the dominant one. Mazallon et al. [24] also studied the breakup regimes of liquid jets injected into a crossflow over a wide range of test conditions and liquid properties. Because our model is for the deformation and trajectory of a liquid column, we limit the scope of the present study to bag/shear and shear breakup regimes. Thus, based on Mazallon et al. [24], the mass stripping in our model starts after meeting the following criteria:

$$(We_{\text{local}} \geq We_{\text{crit}}) \tag{35}$$

where We_{crit} is set to have the value of 60 according to Mazallon et al. and

$$We_{\text{local}} = \frac{\rho_j u_g^2 2a}{\sigma} \tag{36}$$

The equation for mass shedding from the cylindrical element of our model is

$$M_{\text{shed}} = \frac{3}{4}(\pi d)^{3/2}\rho_j \frac{t_{\text{start}}}{t^*} GRHu_g R_M t_{\text{start}} \tag{37}$$

where

$$G = \left(\frac{\rho_g}{\rho_j}\right)^{1/3}\left(\frac{\mu_g}{\mu_j}\right)^{1/3}, \qquad H = \sqrt{\frac{8\mu_j}{3Gu_g}}$$

and t_{start} is the time elapsed from the start of the mass stripping, and t^* is the characteristic aerodynamic time defined as

$$t^* = \frac{d_0\sqrt{\rho_j/\rho_g}}{u_g} \tag{38}$$

Equation (37) is taken from Ranger and Nicholls [25] and Chryssakis and Assanis [26] with two modifications. First, the term t_s/t^* has been added to control the shedding rate to increase essentially linearly with distance away from the start point of stripping [6]. Second, the mass shedding formula is multiplied by the ratio of the element's mass to that of a spherical droplet with the radius r_{eq}. This is due to the fact that the original equation was derived for mass shedding from a liquid drop [25]. Thus, mass ratio R_M in Eq. (31) is

$$R_M = \frac{h\rho_l \pi r_{\text{eq}}^2}{4/3\rho_l \pi r_{\text{eq}}^3} = \frac{3h}{4r_{\text{eq}}} \tag{39}$$

D. Drag Coefficient

Drag coefficient, C_D, plays an important role in the prediction of the jet trajectory. As discussed earlier, it appears in Eq. (29), which calculates the aerodynamic force and thus affects the rotation angle of the liquid column. Various drag coefficients have been proposed for the liquid jets in crossflow. Inamura [16] assumed the value of unity for the drag coefficient which is the value usually used for circular cylinders. Wu et al. [10] suggested an empirical value of 1.696 for the total drag coefficient of liquid jets in subsonic crossflows, and Sallam et al. [27] offered the value of 3 for nonturbulent jets at the shear breakup regime. In this study, drag coefficients are calculated for smooth circular and elliptical elements with the major axis normal to the gas flow at different Reynolds numbers. The gas Reynolds number is defined as

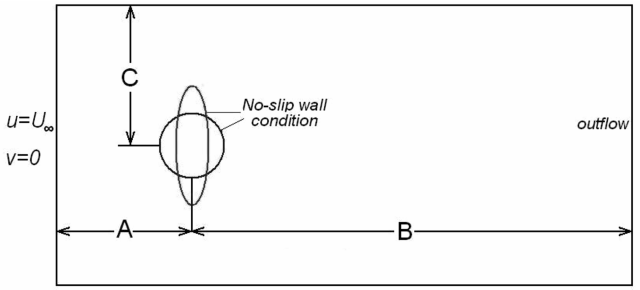

Fig. 4 Computational domain, geometry, and boundary conditions of the drop drag calculation.

$$Re_g = \rho_g u_{\text{rel}} d_{\text{eq}}/\mu_g \tag{40}$$

where $d_{\text{eq}} = 2r_{\text{eq}}$ is the equivalent diameter.

An efficient 2-D numerical method is used to calculate the drag coefficients for different aspect ratios of elements at different flow conditions. It is known that, for long circular cylinders, the flowfield becomes 3-D at $Re \approx 180$. Therefore, for most Reynolds numbers studied here (150–8000), these 2-D results are not applicable to long cylinders. However, because the thickness of the element considered in our model is very small, the 2-D assumption is fairly acceptable. The emphasis is on finding the relationship between the time-averaged drag coefficients and Reynolds number at different aspect ratios and, therefore, details of the flowfield are not discussed here.

The 2-D unsteady Navier-Stokes equations are solved using a finite volume computational fluid dynamics (CFD) code [28]. The governing equations are discretized and solved in a segregated manner using second-order accurate spatial and implicit temporal schemes. The laminar calculations are performed for Reynolds numbers below 1000, and the Spalart–Allmaras [29] one-equation turbulence model is used in turbulence calculations for higher Reynolds numbers. The computational domain size, boundary conditions, and number of computational cells for all three cases are shown in Fig. 4 and Table 1.

The inlet, upper, and lower boundaries are located far enough from the element to minimize the effects of boundaries on the flow around the object and on the drag coefficient calculations. The outlet boundary is located far enough downstream of the cylinder to eliminate the far-field effects on the near wake and to allow for development of the vortical structures.

The numerical calculations are carried out on a nonuniform structured grid. To capture the vortical structures in the wake of the cylinder, the grid is refined near the cylinder wall and downstream of the cylinder. The distance of the first grid point from the cylinder wall is chosen to be 0.2% of the cylinder equivalent diameter d_{eq}. The simulations are performed for three different aspect ratios of $e = 1$, 0.5, and 0.25 and six different Reynolds numbers of $Re = 150$, 500,

Table 1 Computational domain size and number of cells used for different cases

Case	A	B	C	Number of cells
$e = 1$	$7.5d_{\text{eq}}$	$20d_{\text{eq}}$	$12.5d_{\text{eq}}$	130,500
$e = 0.5$	$15d_{\text{eq}}$	$50d_{\text{eq}}$	$20d_{\text{eq}}$	185,300
$e = 0.25$	$15d_{\text{eq}}$	$50d_{\text{eq}}$	$20d_{\text{eq}}$	482,240

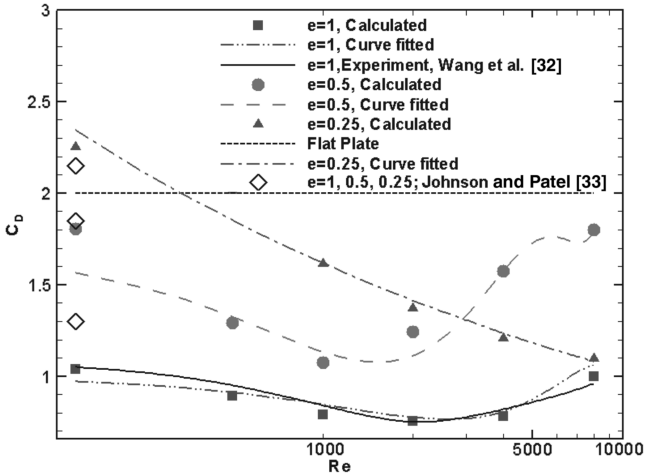

Fig. 5 Calculated drag coefficients versus Reynolds number compared with Wang et al. [32] and Johnson and Patel [33].

1000, 2000, 4000, and 8000. The calculated average drag coefficients are plotted versus the Reynolds number in Fig. 5.

It is known that, for a circular cylinder, as the Reynolds number increases, the drag coefficient first reduces slightly and then increases after a turning Reynolds number, where the drag coefficient is minimum. A similar trend can be observed for the elliptical elements of $e = 0.5$ with the turning Reynolds number shifting toward the smaller values. For $e = 0.25$, however, the drag coefficient continuously decreases with increasing the Reynolds number. At lower Reynolds numbers, a decrease in the aspect ratio results in an increase in the drag coefficient, as can be observed in Fig. 5. However, this does not hold true for Reynolds numbers larger than 3000, as the $e = 0.25$ case does not follow the trend. The equations for the curves fitted to the drag data are presented in Eqs. (41–44). It should be noted that the suggested curves only apply to the range of Reynolds numbers of the present study ($150 < Re < 8000$) and for flows where 3-D effects can be neglected. The results may deviate from the actual values when extrapolated and used for Reynolds numbers out of this range.

To apply the results of calculated drag coefficients into the current model, interpolation is needed between the different Reynolds numbers and different aspect ratios. Because our calculations are limited to a minimum aspect ratio of $e = 0.25$, a lower limit for interpolation is needed. The shape of the jet cross section becomes nearly a flat plate as the aspect ratio decreases below 0.25 and, thus, the drag coefficient of the flow past a normal infinite flat plate is set to be the lower limit. For a 2-D normal flat plate of infinite aspect ratio, C_D is 1.98 [30,31].

The following are the equations for the curves fitted to the data points:

$$e = 1:\ C_D = (-3.46 \times 10^{-12})Re^3 + (5.22 \times 10^{-8})Re^2 - (2.01 \times 10^{-4})Re + 1.0 \tag{41}$$

$$e = 0.5:\ C_D = (3.83 \times 10^{-15})Re^4 - (7.37 \times 10^{-11})Re^3 + (4.66 \times 10^{-7})Re^2 - (9.62 \times 10^{-4})Re + 1.7 \tag{42}$$

$$e = 0.25:\ C_D = 6.22Re^{-0.1949} \tag{43}$$

$$e \le 0.1:\ C_D = 1.98 \tag{44}$$

The results of Wang et al. [32] and Johnson and Patel [33] for a circular cylinder are also shown in Fig. 5 for comparison. The value of the drag coefficient at each time step in the model will be computed by first calculating the Reynolds number and then interpolating linearly between the preceding curves according to the values of the instantaneous aspect ratio e. For aspect ratios smaller than 0.1, the drag coefficient is assumed to be 1.98 as of the flat plate.

E. Summary of the Equations

Equations (27), (30), (31), and (33) are integrated simultaneously using the fourth-order Runge–Kutta method with time steps smaller than 10^{-6} s. Equation (27) solves for the deformation of the cross section, and Eq. (33) solves for θ, the deflection angle. Finally, Eqs. (30) and (31) are integrated to determine the X and Z coordinates of the center of mass of the elliptical element versus time. The calculation of each trajectory takes less than 2 s on a Pentium 4 machine. The following transformations are applied to transfer the coordinates from the center of mass of the element to the upper boundary of the liquid jet, which represents the jet penetration (Fig. 2b):

$$X_{\text{ub}} = r_0 + X_{\text{cm}} - b\cos(\theta) \tag{45}$$

$$Z_{\text{ub}} = Z_{\text{cm}} + b\sin(\theta) \tag{46}$$

The subscripts ub and cm correspond to "upper boundary" and "center of mass," respectively.

IV. Results and Discussions

The effects of different parameters such as nozzle diameter, momentum ratio, gas Weber number, mass stripping, and the drag coefficient on the jet penetration and deformation will be discussed in this section.

A. Jet Deformation

Figure 6 plots the nondimensional deformation of the cross-stream axis a/r_0 versus the Weber number at the onset of breakup, and compares the results with those of Mazallon et al. [24]. The onset of breakup is calculated by [24]

$$\frac{t_i}{t^*} = 8.76We^{-0.62} \tag{47}$$

Calculations are performed for ethanol and water with the momentum ratios in the range of $(9.3 < q < 150)$ for ethanol and $(3.9 < q < 72.5)$ for water. The nozzle diameter is 0.5 mm for all the calculations, and the jet velocity is fixed at 11.8 m/s while changing the Weber number by increasing the gas velocity.

Previous studies have discussed the analogy between the deformation and breakup of the liquid column to that of a liquid droplet. Thus far, several characteristics of the liquid droplet deformation and breakup (DDB) model have been extended and used in the JICF studies. Figure 7 compares the calculated deformation of the liquid jet using the present model with those of the 3-D droplet

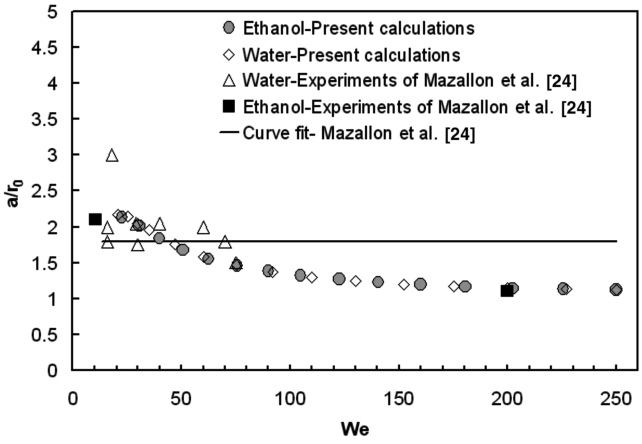

Fig. 6 Calculated nondimensional deformation of the major axis of the jet cross section at the onset of breakup compared with the experimental values (Mazallon et al. [24]).

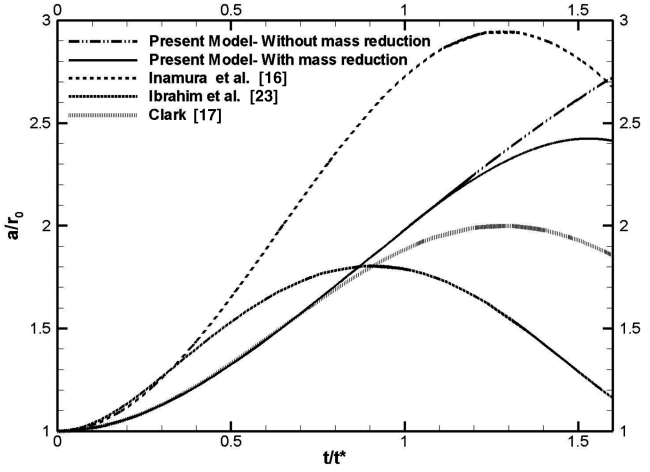

Fig. 7 Comparison of the calculated deformation of the liquid jet using present model with those for the 3-D drop using the DDB model of Ibrahim et al. [23], 2-D drop of Clark [17], and the jet model of Inamura [16]; Water and air at normal temperatures and pressure (NTP), $V_j = 11.8$ m/s, $U_{\text{air}} = 60$ m/s.

calculated using the DDB model of Ibrahim et al. [23], 2-D droplet of Clark [17], and the jet model used by Inamura [16]. The calculations are for water and air at normal temperature and pressure with jet velocity of 11.8 m/s and gas velocity of 60 m/s. The jet (droplet) diameter is 0.5 mm. Comparing the corresponding curves of Ibrahim et al. [23] and Clark [17] shows that, as expected, a 2-D droplet has larger maximum amplitude and frequency of oscillation compared to an axisymmetric droplet in the same flow conditions. A close look at the corresponding curve of the Inamura [16] model shows that the droplet deforms much larger compared to our present model, which is mainly due to the fact that the gas velocity was not projected onto the plane of the element in his study. The calculated curve for the same conditions without considering the mass stripping is also included in the figure to show the effect of mass reduction on the deformation. It is apparent that neglecting the mass stripping leads to overestimation of the jet deformation and, thus, an overprediction of the drag force, which leads to exaggerated deflection of the liquid column.

B. Effect of Momentum Ratio

Figure 8 shows a 3-D view of the jet deformations near the nozzle for three cases with different momentum ratios. At lower momentum ratios, the jet deforms and bends more at lower heights due to the relatively large aerodynamic force. With an increase in q, the jet

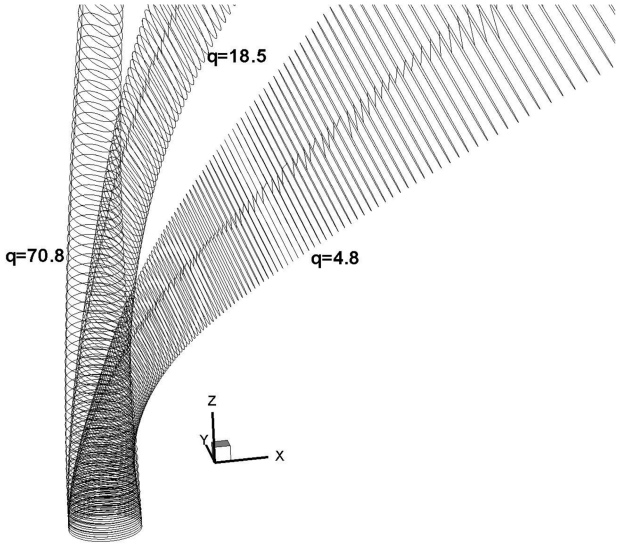

Fig. 8 Near-nozzle deformations of the jets with different momentum ratios.

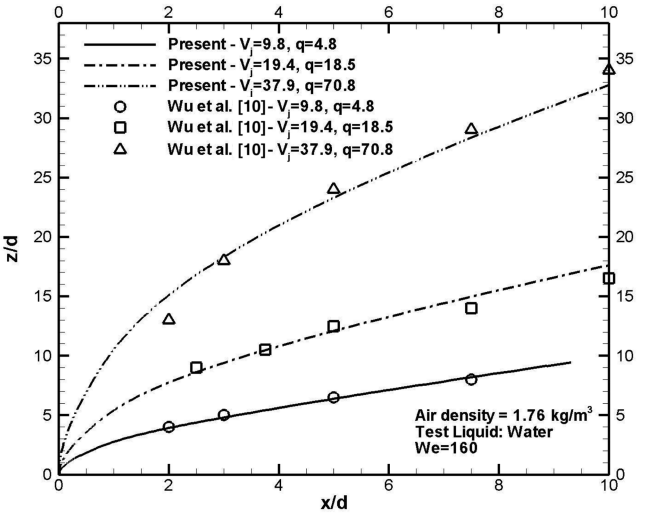

Fig. 9 Calculated trajectories for the cases of Fig. 8 in comparison with the experiments (Wu et al. [10]).

deformation grows large at higher elevations compared with the first case. This allows for the jet to penetrate further into the gas stream. Figure 9 compares the calculated trajectories for the cases of Fig. 8 with the experimental results of Wu et al. [10]. As discussed in the previous studies, the momentum ratio is one of the governing parameters affecting the trajectory of a liquid jet injected normal to a gas stream. However, as will be shown in the next sections, it is not the only factor that controls the jet path. Figure 10 compares the calculated trajectory for one of the cases of Fig. 9 with the experimental result of Wu et al. [10] and the empirical correlations offered by Chen et al. [9], Becker and Hassa [18], and Wotel et al. [34]. The corresponding curve of our model agrees well with the experimental values of Wu et al. [10] and with the correlations of Becker and Hassa [18] and of Wu et al [10]. As observed in Figs. 9 and 10, the present model agrees mostly with the results of Wu et al. [10]. The main reason behind this is the close agreement between the numerically calculated drag coefficient of the present model and the empirical value found by Wu et al. This agreement will be discussed in more detail in Sec. IV.D. The choice of other parameters, such as the critical Weber number and the rate of mass stripping [Eqs. (35) and (37)], also plays a considerable part in the agreement of the results with those of Wu et al.

Figure 11 plots the calculated trajectories for four high-pressure cases and compares them with the MIE-scattering penetration measurements of Rachner et al. [4]. The conditions for the curves of

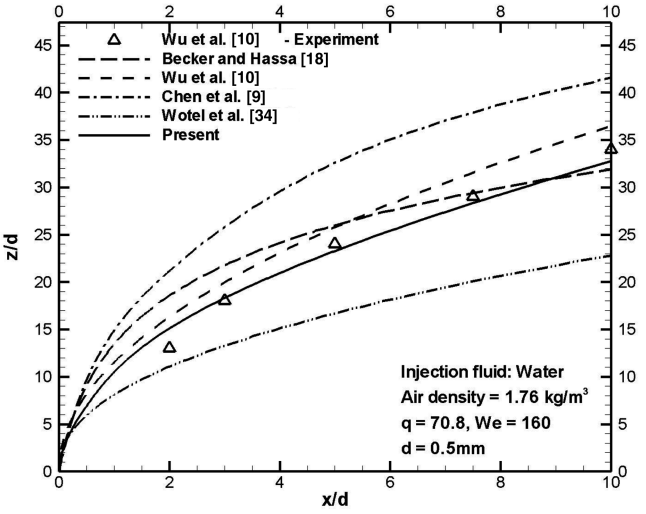

Fig. 10 Comparison between the jet trajectories obtained from the present model with some available correlations and experiment of Wu et al. [10].

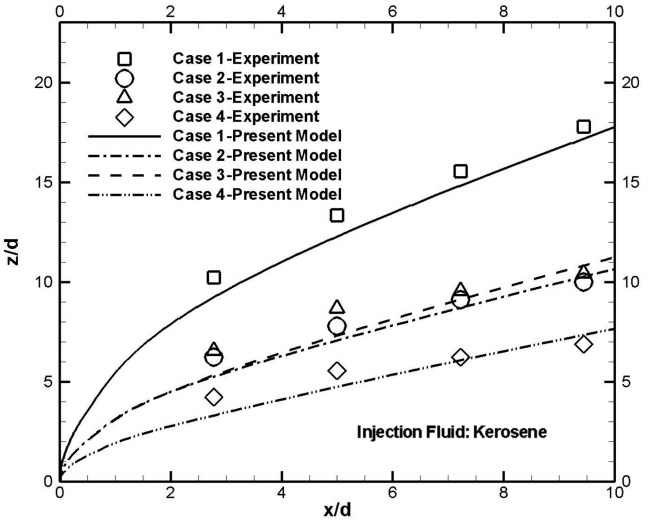

Fig. 11 Calculations for high pressure cases in comparison with experiments of Rachner et al. [4]. The test conditions for cases are summarized in Table 2.

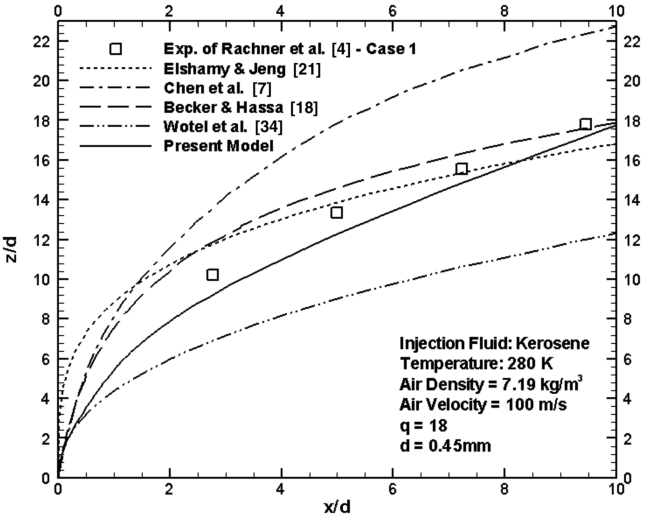

Fig. 12 Comparison of the present calculation for the first case of Fig. 11 with some correlations.

Fig. 11 are exactly those of Rachner et al., and the details are summarized in Table 2. Comparing Fig. 11 in this paper with Fig. 4 of Rachner et al. shows a surprisingly close agreement between the calculations of the present model and the calculations of the model presented by Rachner et al. However, both calculations slightly underestimate the penetration. From our model's point of view, this underprediction might be due to the fact that, at higher pressures, the mass reduction equation used in the current model underestimates the mass stripped from the liquid column. This leads to a larger frontal area of the deformed element (because of the excess mass), which leads to an exaggerated drag force and thus deflects the jet slightly more. Another possible reason is that, at higher pressures, the drag coefficients of liquid droplets and jets are smaller than those of rigid bodies, as reported by Czerwonatis and Eggers [35]. This is mainly due to the effects of surface tension changes at high pressures and also the surface roughness created by surface breakup [35]. So, the present drag coefficients calculated for rigid smooth elliptical elements can also contribute to the deviation observed in Fig. 11. Figure 12 compares the calculated trajectory for a case of high pressure (5.8 bars) with some empirical correlations. It should be noted that the two empirical correlations used in Fig. 12, offered by Elshamy and Jeng [21] and Becker and Hassa [18], were specifically derived for high pressures and thus better agree with the experimental values. This reemphasizes the importance of considering the flow conditions in choosing a correlation.

C. Effect of Weber number

As discussed earlier, the momentum ratio is not the only parameter in calculating the jet trajectory. Gas Weber number can also have considerable effects on the jet penetration because it governs the start and rate of mass shedding from the liquid column. Therefore, incorporating the Weber number in a penetration model or correlation has a positive contribution and also brings the liquid phase surface tension into account.

Figure 13 shows the variation in the jet trajectory as the Weber number increases at a constant liquid-to-gas momentum ratio. The

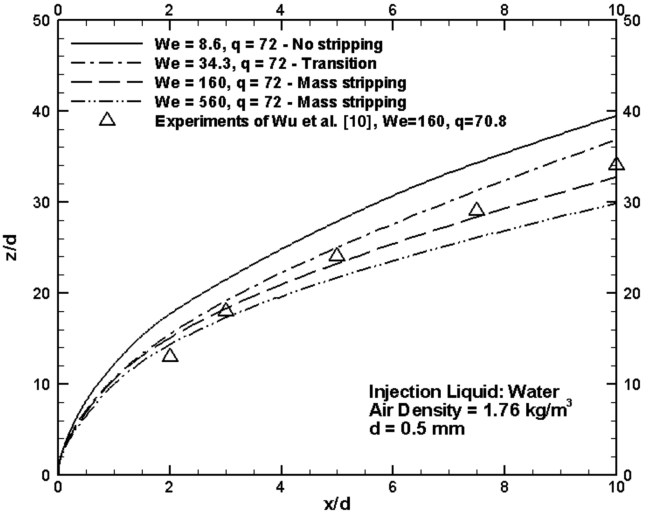

Fig. 13 Effect of Weber number on the trajectory at a constant momentum ratio using the present model. The experimental data of Wu et al. [10] for $We = 160$ are also plotted for comparison.

Weber number is increased by increasing the gas velocity, and the jet velocity is also increased in such a way that the momentum ratio remains constant. The term "no stripping" for the case with $We = 8.6$ refers to the fact that the local Weber number for this test case does not pass the criteria of Eq. (35). The term "transition" refers to the fact that the local Weber number exceeds the critical limit somewhere on the jet trajectory, and the stripping starts at some location downstream of the injection point. The term "mass stripping" refers to the fact that the jet is in the shear breakup and the local Weber number is initially above the criteria and, thus, mass is stripped off the column from the injection point. Increasing the Weber number by changing the gas velocity affects the trajectory calculations in two ways. First, it changes the gas-phase Reynolds

Table 2 Test conditions for the cases of Figs. 11 and 12 [4]

Case no.	Air pressure, bar	Air temp., K	Air density, kg/m^3	Air velocity, m/s	q
1	5.8	280	7.19	100	18
2	8.7	280	10.78	100	6
3	5.9	285	7.18	75	6
4	5.9	285	7.18	75	2

number. This changes the drag coefficient and thus the aerodynamic force exerted on the jet. Second, it changes the critical Weber number and the rate of mass stripping which can affect the jet trajectory, as will be explained in Sec. IV.E. Figure 13 shows how these parameters can change the jet penetration. This variation is also shown in Fig. 14 where the penetration curves for the same cases are plotted using the empirical correlation offered by Elshamy and Jeng [21] [Eq. (13)]. Their correlation includes a term for gas Weber number as well as pressure and momentum ratio. Although the trajectories are not exactly the same as those of Fig. 13, both figures demonstrate similar trajectory variations with an increase in Weber number.

D. Effect of Drag Coefficient

Figure 15 shows the jet trajectories calculated for a case with the momentum ratio of 72 and gas Weber number of 140. There are three curves in the figure, two of which have been obtained using a constant drag coefficient. The first curve is calculated using the adaptive C_D scheme of the present model [Eqs. (41–44)]. The second and third curves are computed using a constant C_D value of 1.0 used by Inamura et al. [16] and the empirical value of 1.7 from Wu et al. [10], respectively. The former obviously leads to overestimation of the jet penetration, as it underpredicts the drag force and also does not take into account the deformation of the liquid jet and the variation in the Reynolds numbers due to change in u_{rel} and d_{eq} [Eq. (40)]. The calculated trajectory from the present model, which is obtained using the numerically calculated C_D, is in good agreement with the trajectory obtained using the empirical C_D value of 1.7 given by Wu et al. [10]. This implies that the calculated drag coefficients of the present model are close to the experimental values. As mentioned earlier, this, we believe, is the main reason behind close agreement of our jet penetration results with those of Wu et al. Table 3 contains the time-averaged drag coefficients obtained for different test cases. The average values are in the range of 1.6–1.7, which is consistent with the empirical value.

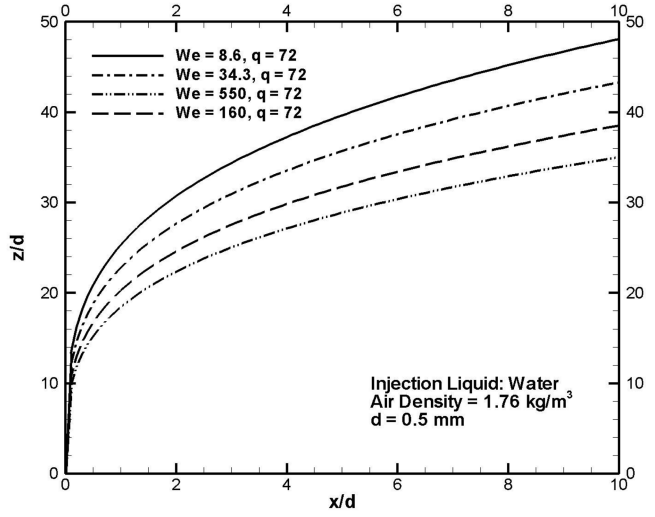

Fig. 14 Effect of Weber number on the trajectory at constant momentum ratio using the empirical correlation of Elshamy and Jeng [21].

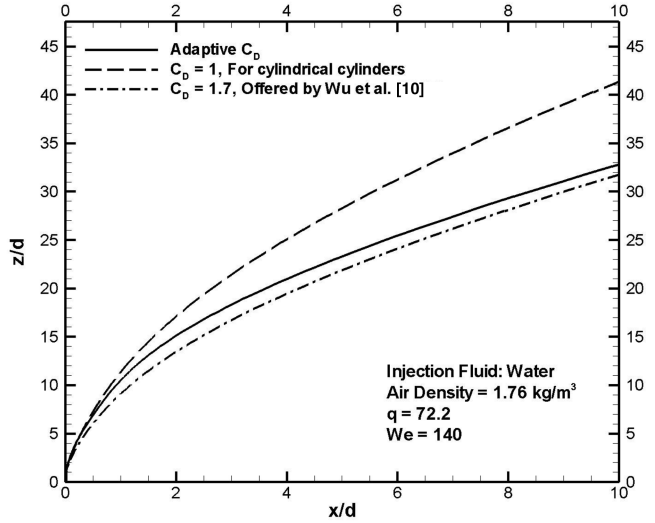

Fig. 15 Comparison between trajectories obtained using the adaptive C_D scheme of the present model and constant C_D values.

Table 3 Time-averaged drag coefficients calculated for different cases

Case no.	We	q	Time-averaged C_D
1	34	72	1.58
2	140	72	1.6
3	71	9.9	1.61
4	139	9.4	1.65
5	281	10	1.68

E. Effect of Mass Stripping

Mass stripping is incorporated in the present model in the form of a decrease in the jet cross section, that is, a decrease in the equivalent radius. This change in the cross section is strongly dependant on the gas Weber number and has a considerable effect on the drag force. To illustrate how Eqs. (35) and (36) control the start of mass stripping, Fig. 16 plots the local Weber number versus the nondimensional time [Eq. (38)] for three cases with different gas velocities. The jet velocity is kept constant for all the cases. Figure 17 also illustrates the corresponding variation in the ratio of the stripped mass and the nondimensional time for the cases of Fig. 16. As Fig. 16 depicts, for the first curve with gas velocity of 50 m/s, the local Weber number does not exceed the stripping limit line. Thus, no mass would be removed from the column in the present model, as shown by the corresponding curve in Fig. 17. For the second case, the local Weber number exceeds the limit at the nondimensional time of almost 0.6 and, as Fig. 17 shows, mass stripping would start after this point smoothly from zero. For the third case with gas velocity of 90 m/s, the mass is removed from the column right from the injection point because its local Weber number starts from the value of nearly 70, which is initially above the limit of $We_{crit} = 60$.

To better demonstrate the effect of mass stripping on the trajectory, Fig. 18 shows the deformation of the column cross section for a case with Weber number of 67, water jet velocity of 20 m/s, air density of 1.2 kg/m^3, and nozzle diameter of 0.5 mm. Figure 18a

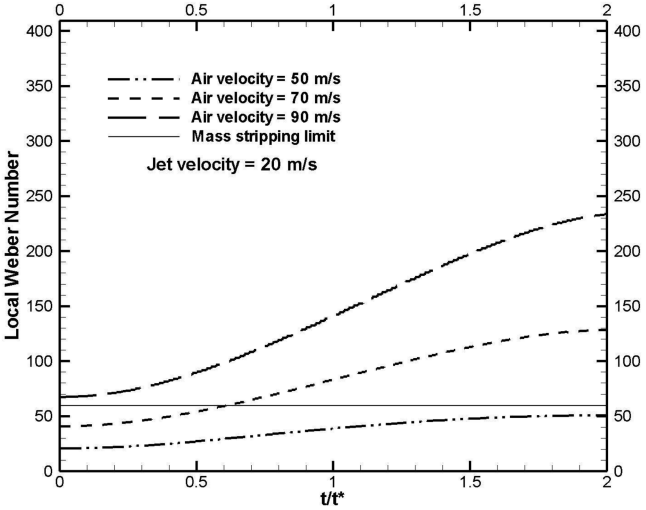

Fig. 16 Growth of the local Weber number versus time for three jets at different breakup regimes.

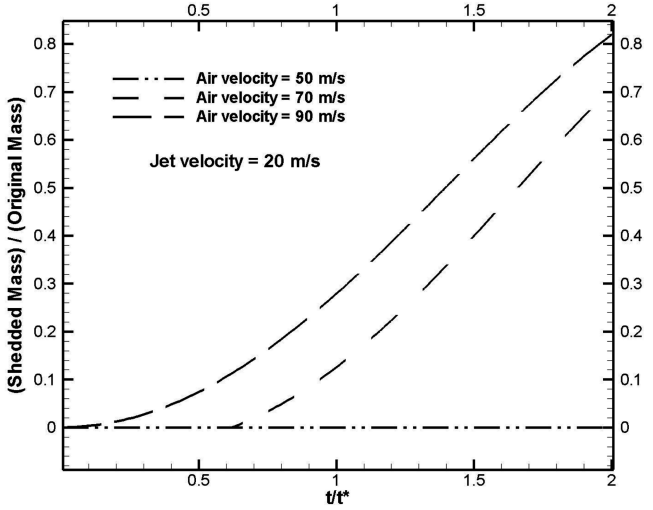

Fig. 17 Ratio of the mass stripped from the elliptic element versus time for the cases of Fig. 16.

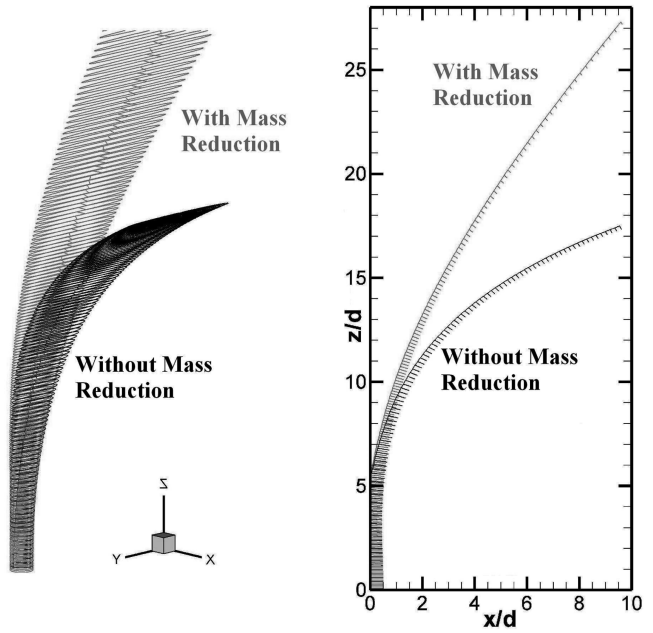

Fig. 18 Deformation of jet cross section with and without mass shedding model for a case with Weber number of 67, water and air at NTP, $V_j = 20$ m/s, $U_{air} = 90$ m/s, and nozzle diameter of 0.5 mm: a) 3-D view, b) side view.

depicts the effect of mass reduction on the estimated liquid jet shape. Because the initial Weber number is above the stripping criteria, the mass stripping has a considerable effect on the penetration. Figure 18b shows the side view of the jets, and Fig. 19 compares the deformed cross sections for both cases from the top view. Neglecting the mass stripping leads to overprediction of the cross-sectional deformation and the drag force (due to the excess mass). This results in overestimation of the jet deflection, as shown in Fig. 18.

F. Effect of the Nozzle Diameter

Most of the correlations mentioned in the Introduction are nondimensionalized by the nozzle diameter. Therefore, they simply suggest that the change in the nozzle diameter does not affect the jet path as long as the trajectory is plotted in a nondimensionalized coordinate system. To investigate the validity of this assumption, Fig. 20 compares the jet penetrations for three cases with different nozzle diameters. The momentum ratio and gas Weber numbers are held constant by changing the jet and gas velocities to merely investigate the effect of the nozzle diameter. An 8% difference in the penetration height can be observed when the diameter is increased from 0.5 to 2 mm. Bearing in mind that the jet surface in real conditions is far from smooth, this relatively small error is acceptable. Figure 21 plots the trajectories for three cases where the

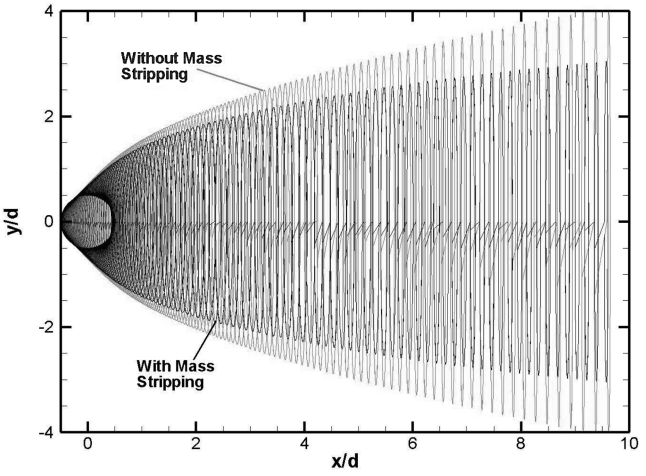

Fig. 19 Top view of the jet deformations for the cases of Fig. 18.

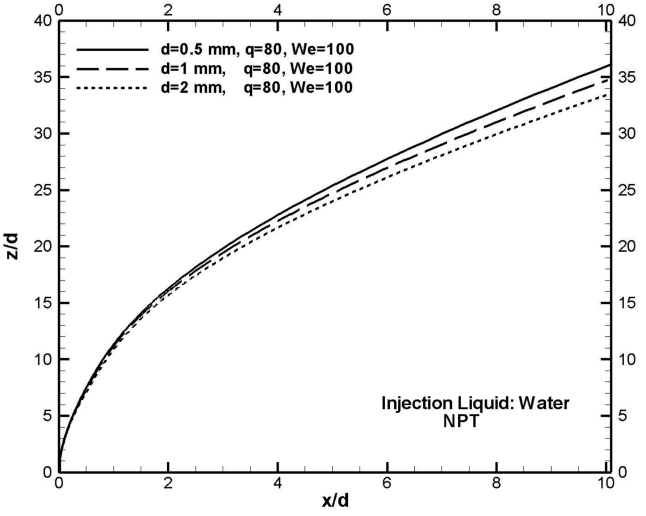

Fig. 20 Effect of the nozzle diameter at constant momentum ratio and Weber number. The jet and gas velocities are varied to keep q and We constant.

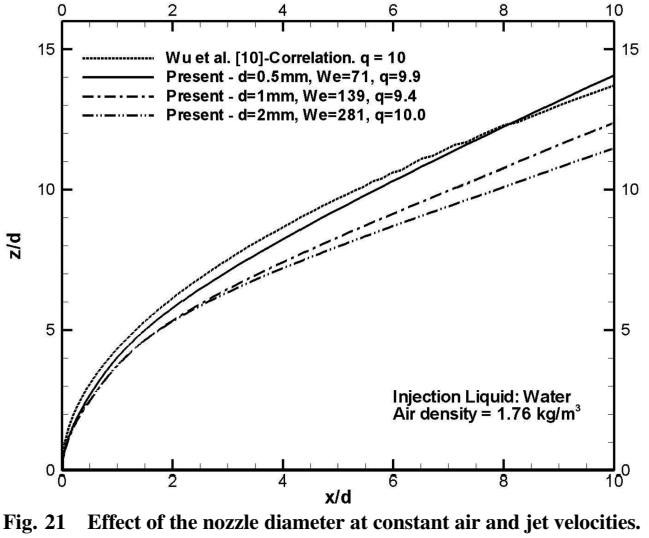

Fig. 21 Effect of the nozzle diameter at constant air and jet velocities.

gas and jet velocities are kept constant and the nozzle diameter is varied. Because the jet and gas velocities are constant, the momentum ratio remains constant. However, the Weber number grows larger with an increase in the nozzle diameter, which affects the mass stripping submodel and the drag coefficient. As Fig. 21 shows, this type of increase in the Weber number also leads to smaller jet penetrations, similar to Figs. 13 and 14, where the Weber number was increased by changing the gas velocity. Figures 20 and 21 suggest that, as long as the Weber number and the momentum ratios are held constant, the jet trajectory is not affected much when plotted in a coordinate system which is non-dimensionalized by d. However, if the Weber number changes by changing d, as shown in Fig. 21, the change in the trajectory becomes considerable.

V. Conclusions

Deformation and trajectory of a liquid jet in uniform gaseous crossflow is modeled and compared with some experimental and theoretical data available in the literature. The results suggest the following:

1) The jet cross-sectional deformation plays a great role in predicting the trajectory because it significantly affects the drag force exerted on the column. A good approximation of the deformation evolution is necessary for accurate prediction of other characteristics of the liquid jet in crossflows.

2) Assuming a constant drag coefficient in calculation of the jet penetration neglects the effect of deformation on the drag force and leads to errors in the calculations. An adaptive drag scheme is needed to capture the correct trend of the liquid trajectory. The drag coefficient data offered in this study have been calculated using a CFD code for the Reynolds numbers of 200–8000 and aspect ratios of 1–4.

3) It is shown that calculation of the aerodynamic drag force on the liquid column, using the local projected gas velocity u_{rel} and the locally calculated drag coefficient, provides a close approximation for the drag force of the liquid column. This is confirmed by the fact that the time-averaged drag coefficients calculated are in the range of 1.6–1.7, which are in good agreement with the empirical value.

4) In addition to the liquid-to-gas momentum ratio, the Weber number also plays an important role in the penetration and atomization of the liquid jets in crossflows. It affects the onset of mass stripping, the rate of shedding, and the breakup regime. A local Weber number based on the instantaneous cross-stream axis of the jet cross section has been defined. This definition enables control of the start of the mass stripping from the liquid column, allowing it to start at different heights of the jet depending on the flow conditions and not necessarily from the injection point.

5) Mass stripping plays an important role in predicting the jet penetration because it changes the jet cross section and affects the drag force on the jet column. As the mass of the liquid element decreases, the ratio of its momentum to the gas momentum decreases and the jet tends to bend and deform more. Thus, the rate of mass stripping plays an important role on the jet trajectory. As the Weber number grows, these effects become more evident, especially around the transition Weber number, which corresponds to the onset of mass striping.

6) The presented theoretical model is applicable to a wide range of flow conditions and has minimal computational cost. The results are quite sensitive to the choice of the critical Weber number, the equation used for the rate of mass stripping, and the numerically obtained correlations for the drag coefficient. However, no fine tuning was done in the presented results to match the calculations with correlations and experiments.

Acknowledgments

This work is partly supported by Natural Sciences and Engineering Research Council of Canada, Natural Resources Canada, and AUTO21 Network of Centers of Excellence.

References

[1] Reitz, R. D., "Modeling Atomization Processes in High-Pressure Vaporizing Sprays," *Atomization and Sprays*, Vol. 3, No. 4, 1987, pp. 309–339.

[2] Liu, F., Smallwood, G. J., and Gülder, Ö. L., "Numerical Study of Breakup Processes of Water Jet Injected into a Cross Air Flow," *Proceedings of the 8th Annual Conference on Liquid Atomization and Spray Systems*, Inst. for Liquid Atomization and Spray Systems, July 2000, pp. 67–74.

[3] O'Rourke, P. J., and Amsden, A. A., "The TAB Method for Numerical Calculation of Spray Droplet Breakup," Society of Automotive Engineers Paper 872089, 1987.

[4] Rachner, M., Becker, J., Hassa, C., and Doerr, T., "Modeling of the Atomization of a Plain Liquid Fuel Jet in Crossflow at Gas Turbine Conditions," *Aerospace Science and Technology*, Vol. 6, No. 7, 2002, pp. 495–506.
doi:10.1016/S1270-9638(01)01135-X

[5] Madabhushi, R. K., "A Model For Numerical Simulation of Breakup of a Liquid Jet in Crossflow," *Atomization and Sprays*, Vol. 13, No. 4, 2003, pp. 413–424.
doi:10.1615/AtomizSpr.v13.i4.50

[6] Khosla, S., and Crocker, D. S., "CFD Modeling of the Atomization of Plain Liquid Jet in Crossflow for Gas Turbine Applications," American Society of Mechanical Engineers Turbo Expo Paper GT2004-54269, June 2004.

[7] Lin, K. C., Kennedy, P. J., and Jackson, T. A., "A Review on Penetration Heights of Transverse Liquid Jets in High Speed Flows," *15th Annual Conference on Liquid and Atomization and Spray Systems*, Inst. for Liquid Atomization and Spray Systems [CD-ROM], May 2002.

[8] Schetz, J. A., and Padhye, A., "Penetration and Breakup of Liquids in Subsonic Airstreams," *AIAA Journal*, Vol. 15, No. 10, 1977, pp. 1385–1390.
doi:10.2514/3.60805

[9] Chen, T. H., Smith, C. R., Schommer, D. G., and Nejad, A. S., "Multi-Zone Behavior of Transverse Liquid Jet in High-Speed Flow," *31st Aerospace Sciences Meeting and Exhibit*, AIAA Paper 93-0453, 1993.

[10] Wu, P. K., Kirkendall, K. A., Fuller, R. P., and Nejad, A. S., "Breakup Processes of Liquid Jets in Subsonic Crossflow," *Journal of Propulsion and Power*, Vol. 13, No. 1, 1997, pp. 64–73.
doi:10.2514/2.5151

[11] Wu, P. K., Kirkendall, K. A., Fuller, R. P., and Nejad, A. S., "Spray Structures of Liquid Jets Atomized in Subsonic Crossflows," *Journal of Propulsion and Power*, Vol. 14, No. 2, 1998, pp. 173–182.
doi:10.2514/2.5283

[12] Inamura, T., Nagai, N., Watanabe, T., and Yatsuyanagi, N., "Disintegration of Liquid and Slurry Jets Traversing Subsonic Airstreams," *Proceedings of the 3rd World Conference on Experimental Heat Transfer, Fluid Mechanics and Thermodynamics*, Elsevier, Amsterdam, 1993, pp. 1522–1529.

[13] Heister, S. D., Nguyen, T. T., and Karagozian, A. R., "Modeling of Liquid Jets Injected Transversely into a Supersonic Crossflow," *AIAA Journal*, Vol. 27, No. 12, 1989, pp. 1727–1734.
doi:10.2514/3.10327

[14] Li, H. S., and Karagozian, A. R., "Breakup of a Liquid Jet in Supersonic Crossflow," *AIAA Journal*, Vol. 30, No. 7, 1992, pp. 1919–1921.
doi:10.2514/3.11157

[15] Nguyen, T. T., and Karagozian, A. R., "Liquid Fuel Jet in Subsonic Crossflow," *Journal of Propulsion and Power*, Vol. 8, No. 1, 1992, pp. 21–29.
doi:10.2514/3.23437

[16] Inamura, T., "Trajectory of a Liquid Jet Traversing Subsonic Airstreams," *Journal of Propulsion and Power*, Vol. 16, No. 1, 2000, pp. 155–157.
doi:10.2514/2.5547

[17] Clark, M. M., "Drop Breakup in a Turbulent Flow, I: Conceptual and Modeling Considerations," *Chemical Engineering Science*, Vol. 43, No. 3, 1988, pp. 671–679.
doi:10.1016/0009-2509(88)87025-8

[18] Becker, J., and Hassa, C., "Breakup and Atomization of a Kerosene Jet in Crossflow at Elevated Pressure," *Atomization and Sprays*, Vol. 12, Nos. 1–3, 2002, pp. 49–67.
doi:10.1615/AtomizSpr.v12.i123.30

[19] Masuda, B. J., Hack, R. L., McDonell, V. G., Oskam, G. W., and Cramb, D. J., "Some Observations of Liquid Jet in Crossflow," *18th Annual Conference on Liquid and Atomization and Spray Systems*, Inst. for Liquid Atomization and Spray Systems [CD-ROM], 2005.

[20] Lakhamraju, R. R., and Jeng, S. M., "Liquid Jet Breakup Studies in Subsonic Air Stream at Elevated Temperatures," *18th Annual Conference on Liquid and Atomization and Spray Systems*, Inst. for Liquid Atomization and Spray Systems [CD-ROM], 2005.

[21] Elshamy, O. M., and Jeng, S. M., "Study of Liquid Jet in Crossflow at Elevated Ambient Pressures," *18th Annual Conference on Liquid and Atomization and Spray Systems*, Inst. for Liquid Atomization and Spray Systems [CD-ROM], 2005.

[22] Stenzler, J. N., Lee, J. G., and Santavicca, D. A., "Penetration of Liquid Jets in a Cross-Flow," *Atomization and Sprays*, Vol. 16, No. 8, 2006, pp. 887–906. doi:10.1615/AtomizSpr.v16.i8.30

[23] Ibrahim, E. A., Yang, H. Q., and Przekwas, A. J., "Modeling of Spray Droplets Deformation and Breakup," *Journal of Propulsion and Power*, Vol. 9, No. 4, 1993, pp. 651–654. doi:10.2514/3.23672

[24] Mazallon, J., Dai, Z., and Faeth, G. M., "Primary Breakup of Nonturbulent Round Liquid Jets in Gas Crossflows," *Atomization and Sprays*, Vol. 9, No. 3, 1999, pp. 291–312.

[25] Ranger, A. A., and Nicholls, J. A., "Aerodynamic Shattering of Liquid Drops," *AIAA Journal*, Vol. 7, No. 2, 1969, pp. 285–290. doi:10.2514/3.5087

[26] Chryssakis, C. A., and Assanis, D. N., "A Secondary Atomization Model for Liquid Droplet Deformation and Breakup Under High Weber Number Conditions," *18th Annual Conference on Liquid and Atomization and Spray Systems*, Inst. for Liquid Atomization and Spray Systems [CD-ROM], 2005.

[27] Sallam, K. A., Aalburg, C., and Faeth, G. M., "Breakup of Round Nonturbulent Liquid Jets in Gaseous Crossflow," *AIAA Journal*, Vol. 42, No. 12, 2004, pp. 2529–2540. doi:10.2514/1.3749

[28] Computational Fluid Dynamics (CFD) Software, User Manual, Ver. 6.0 (2), Fluent, Lebanon, NH, 2002

[29] Spalart, P. R., and Allmaras, S. R., "A One-Equation Turbulence Model for Aerodynamic Flows," *30th AIAA Aerospace Sciences Meeting and Exhibit*, AIAA Paper 92-0439, 1992.

[30] Ringuette, M. R., "Vortex Formation and Drag on Low Aspect Ratio, Normal Flat Plates," Ph.D. Dissertation, Mechanical Engineering Dept., California Inst. of Technology, Pasadena, CA, 2004.

[31] McCormick, B. W., *Aerodynamics, Aeronautics, and Flight Mechanics*, 2nd ed., Wiley, New York, 1995.

[32] Wang, M., Catalano, P., and Iaccarino, G., "Prediction of High Reynolds Number Flow over a Circular Cylinder Using LES with Wall Modeling," *Annual Research Briefs*, Center for Turbulence Research, Stanford Univ., Stanford, CA, 2001.

[33] Johnson, T. A., and Patel, V. C., "Flow past a Sphere up to a Reynolds Number of 300," *Journal of Fluid Mechanics*, Vol. 378, Jan. 1999, pp. 19–70. doi:10.1017/S0022112098003206

[34] Wotel, G. J., Gallagher, K. E., Caron, S. D., Rosfjord, T. J., Hautman, D. J., and Spadaccini, L. J., "High Speed Turboramjet Combustor Technology Program," Wright Lab., TR-91-2043, Wright–Patterson AFB, OH, 1991.

[35] Czerwonatis, N., and Eggers, R., "Disintegration of Liquid Jets and Drop Drag Coefficients in Pressurized Nitrogen and Carbon Dioxide," *Chemical Engineering and Technology*, Vol. 24, No. 6, 2001, pp. 619–624. doi:10.1002/1521-4125(200106)24:6<619::AID-CEAT619>3.0.CO;2-H

R. Rangel
Associate Editor